## Spin-polarized lasing in a highly photoexcited semiconductor microcavity

Feng-kuo Hsu, 1, \* Wei Xie, 1, \* Yi-Shan Lee, 2 Sheng-Di Lin, 2 and Chih-Wei Lai 1, †

Lasing in semiconductors is generally independent of the spins of electrons and holes, which constitute the gain medium. However, in a few spin-controlled lasers, spin-polarized carriers with long spin relaxation times ( $\sim$ 1 ns) result in continuous or sub-nanosecond pulsed circularly polarized stimulated emission. In these spin-controlled semiconductor lasers, a spin-imbalanced population inversion has been considered necessary. Here, we demonstrate room-temperature spin-polarized ultrafast ( $\sim$ 10 ps) lasing in a highly optically excited GaAs microcavity embedded with InGaAs multiple quantum wells within which the spin relaxation time is less than 10 ps. The laser radiation remains highly circularly polarized even when excited by nonresonant elliptically polarized light. In contrast to conventional semiconductor lasers, it exhibits a nonlinear input-output relation, energy shifts, and spectral broadening as a function of the photoexcited density. Such spin-polarized lasing is attributed to a spin-dependent stimulated process in a high-density electron-hole plasma coupled to the cavity light field.

Circularly polarized light has been used in various applications, ranging from the determination of protein structures with circular dichroism spectroscopy [1] and stereoscopic image projection in a polarized threedimensional (3D) system to spin-dependent electronics (spintronics) and quantum computation [2]. By controlling nonequilibrium spin dynamics and radiation processes in semiconductors, one can obtain a spin-controlled laser (spin-laser) [3–6] emitting circularly polarized coherent radiation. In semiconductors, spin-polarized electrons (holes) are generated in the conduction (valence) band upon absorption of circularly polarized light above the band-gap, as determined by the optical selection rules [7]. At low photoexcited densities, the photoluminescence (PL) is usually from spontaneous transitions which do not react back on the electron system. In this case, the degree of circular polarization ( $DoCP \equiv \rho_c$ ) of PL reflects the spin polarization in electrons and holes before radiative recombination [7]. When the spin relaxation rate is fast compared to the radiative recombination, the spin polarization in photoexcited carriers (optical orientation) is typically lost during the absorption-cooling cycle, resulting in unpolarized photoluminescence. Similarly,  $\rho_c$  of the emission in spin-controlled light emitting diodes (spin-LEDs) [8] is limited by the electrical spin injection efficiency. Therefore, spin-polarized carriers with a long spin relaxation time  $\tau_s > 100\text{-}1000 \text{ ps}$ have been considered necessary to obtain a spin-laser [3]. Still, highly circularly polarized radiation can result from partially spin-polarized carriers, provided that radiation from a spin-dependent stimulated process dominates [9].

Here, we describe room-temperature spin-polarized sub-10-ps pulsed lasing despite a sub-10-ps electron-spin  $(\tau_s^e)$  and sub-ps hole-spin  $(\tau_s^h)$  relaxation times in the InGaAs/GaAs multiple quantum wells (MQWs) of the microcavity grown on a (100) GaAs substrate. Spin-polarized carriers are optically injected by nonresonant

ps pump pulses at more than 150 meV above the lasing energy. Below threshold, luminescence is unpolarized because  $\tau_s^e \lesssim 10$  ps is short compared to the carrier lifetime  $\tau_n \gtrsim 1$  ns. Under circularly polarized pump, laser action commences above a critical photoexcited density with a high degree of circular polarization, close to unity  $(\rho_c > 0.98)$  (Fig. 1). When excited by nonresonant elliptically polarized pump,  $\rho_c$  of the circularly polarized laser radiation can even exceed that of the pump in the limited photoexcited density regime. Unlike a conventional spin-controlled semiconductor laser [3–6], the spin-polarized laser presented here exhibits a nonlinear input-output relation, energy shifts, and spectral broadening as a function of the photoexcited density. Such spin-polarized states are formed at room temperature, owing to a spin-dependent stimulated process in a highdensity electron-hole (e-h) plasma coupled to the cavity light field.

Coupled electron-hole-photon  $(e-h-\gamma)$  systems are becoming an emerging platform for studies on non-equilibrium collective quantum states. The room-temperature e-h system that we studied consists mainly of free carriers and high-density e-h plasmas as a result of thermal ionization [10]. A many-body state near the Fermi edge in a degenerate high-density e-h system can result in unusual optical properties. For example, Fermi-edge superfluorescence [11] has been observed in a degenerate e-h system, whereas Fermi-edge polaritons [12] or Mahan excitons [13] have been observed in a microcavity containing a 2D electron gas. In this experiment, we explore the high-density regime of a coupled  $e-h-\gamma$  system in which BCS-like states may arise [14, 15].

The  $\lambda$  GaAs/AlAs distributed Bragg reflector (DBR) microcavity studied here has three stacks of three In-GaAs/GaAs MQWs each, embedded at the antinodes of the cavity light field (Supplementary Fig. S1). To investigate laser action in a highly optically pumped microcav-

<sup>&</sup>lt;sup>1</sup>Department of Physics and Astronomy, Michigan State University, East Lansing, MI 48824, USA <sup>2</sup>Department of Electronics Engineering, National Chiao Tung University, Hsinchu 30010, Taiwan (Dated: December 31, 2014)

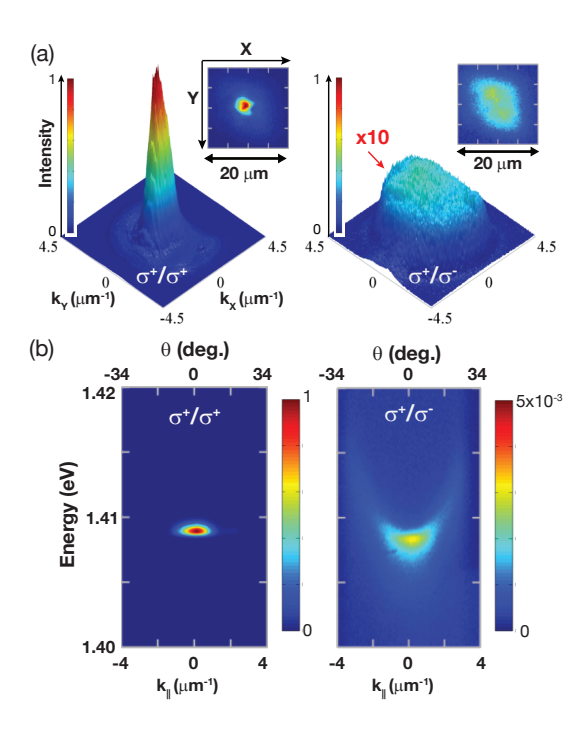


FIG. 1. Spin-polarized lasing at room temperature. (a) Angle-resolved [k-space  $(k_X, k_Y)$ ] luminescence images at lasing threshold  $(P = P_{th})$  for co-circular  $(\sigma^+/\sigma^+, \text{left panel})$  and cross-circular  $(\sigma^+/\sigma^-, \text{right panel})$  components. Here,  $\sigma^{\pm}/\sigma^{\pm}$  represents the polarization of pump/luminescence, respectively.  $P_{th} \approx 2.5 \times 10^8$  photons per pulse (over an area of  $80 \ \mu\text{m}^2$ ), resulting in a photoexcited density  $n_{th} \approx 3 \times 10^{12}$  cm<sup>-2</sup> per QW per pulse for an estimated absorption of 10% for 9 QWs. Insets are corresponding real space (r-space) luminescence images. (b) Energy (E) vs. in-plane momentum  $(k_{\parallel})$  dispersions along  $k_Y$  axis  $(k_X = 0, k_Y = k_{\parallel})$ .

ity, we vary the laser pump flux by two orders of magnitude and create a photoexcited density ranging from approximately  $5 \times 10^{11}$  to  $10^{13}$  cm<sup>-2</sup> per QW per pulse. To control carrier heating and diffusion, we temporally modulated pump intensity and spatially shape the pump laser beam into a flat-top, respectively (see Methods and Supplementary Fig. S3).

We optically pump the sample using 2-ps Ti:Sapphire laser pulses at 1.579 eV ( $\lambda_p=785$  nm), which is near a reflectivity minimum (reflectance  $\approx 40\%$ ) of the microcavity (Supplementary Fig. S2a) and about 170 meV above the lasing energy. For a given threshold photoexcited density  $n_{th}\approx 3\times 10^{12}$  cm<sup>-2</sup> per quantum well, the transient chemical potential ( $\mu$ ) reaches  $\sim 80$  meV above the QW bandgap ( $E_g'\approx 1.33$  eV) and approaches the cavity resonance ( $E_c\sim 1.41$  eV) (see Methods and Supplementary Fig. S5). At low photoexcited density,  $\mu$  is far off-resonant with respect to  $E_c$  and radiative recombination of e-h carriers is largely suppressed.  $\mu$  advances toward  $E_c$  with increasing photoexcited density, resulting in nonlinearly enhanced luminescence efficiency and lasing action eventually.

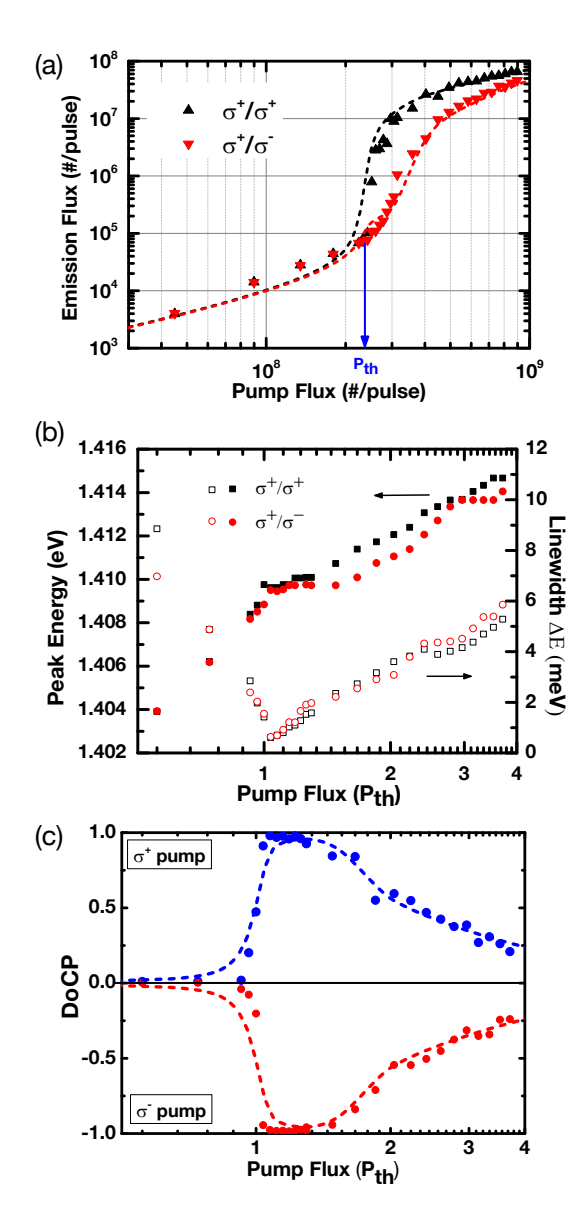


FIG. 2. Photoexcited density dependence. (a) Emission flux integrated over  $|k_{\parallel}| < 3~\mu \mathrm{m}^{-1}$  under a circularly polarized  $\sigma^+$  pump. (b) Spectral linewidths  $\Delta \mathrm{E}$  (FWHM) and peak energies determined from emission spectra (Supplementary Fig. S6). (c) The degree of circular polarization  $DoCP~(\bar{\rho}_c)$ , determined from luminescence integrated near  $k_{\parallel} \approx 0~(|k_{\parallel}| < 0.3~\mu \mathrm{m}^{-1})$  under  $\sigma^+$  or  $\sigma^-$  circularly polarized pump. The dashed lines are calculated emission flux and  $\bar{\rho}_c$  assuming a spin-dependent stimulated process (Supplementary Material).

First, we characterize the laser in terms of the angular distribution and energy as functions of the in-plane momentum [angle-resolved (k-space) images and E vs.  $k_{\parallel}$  dispersions] (Fig. 1). At threshold, the emission of the microcavity studied here becomes angularly and spectrally narrow for the co-circular  $\sigma^+/\sigma^+$  component, where  $\sigma^+/\sigma^+$  is the helicity of the pump/emission, respectively. An intense radiation mode emerges within an

angular spread  $\Delta\theta < 3^\circ$ , corresponding to a standard deviation  $\Delta k = 0.3~\mu\mathrm{m}^{-1}$  in k-space. Approximating such a partially coherent beam as a Gaussian Schell-model source [16], we can determine a spatial coherence length of 4  $\mu\mathrm{m}$ , close to the spatial dimension of the lasing mode (Fig. 1a inset). On the contrary, no lasing action occurs for the cross-circular  $\sigma^+/\sigma^-$  component, which exhibits an angularly broad intensity distribution and a parabolic E vs.  $k_\parallel$  dispersive spectrum. Accordingly, the radiation at threshold has a unity circular polarization.

Next, we describe the nonlinear input-output relation and spectral characteristics. Fig. 2a shows emission flux (output) vs. pump flux (input) under circularly ( $\sigma^+$ ) polarized excitation. Pump flux, P, is the photon flux per pulse transmitted into the microcavity within a circular 10- $\mu m$  diameter area. The output nonlinearly increases by one order of magnitude for an increase of the input by <20% near the critical photoexcited density. The onset of such a nonlinear output for the co-circular component  $(\sigma^+/\sigma^+)$  is defined as the threshold  $P_{th}$  (indicated by an arrow in the figure). The linewidth  $\Delta E$  [full width at half maximum (FWHM)] of the spectral distribution and peak energy of the co- and cross-circularly polarized spectra at  $k_{\parallel} = 0$  under a circularly polarized  $(\sigma^{+})$  pump are plotted in Fig. 2b. When the pump flux is increased from  $P = 0.5 P_{th}$  toward the threshold, luminescence blueshifts by  $\approx 5$  meV, while the linewidth  $\Delta E$  decreases from about 10 meV to 0.3 meV. Slightly above threshold  $(P_{th} < P < 1.5 P_{th})$ , spectrally narrow  $(\Delta E \approx 0.3)$ - 1.0 meV) radiation emerges with a nonlinear growth in magnitude, while the peak energy remains constant. Far above threshold  $(P > 1.5 P_{th})$ , the spectral linewidth increases to more than 2 meV. The overall emission energy shifts with increasing pump flux is more than 10 meV, which is significantly larger than the corresponding energy shift of the cavity stop band (<2 meV) (Supplementary Fig. S2). Additionally, far above threshold, co- and cross-circular components both lase with rising peak energy while retaining an energy splitting of  $\approx 1-2$ meV. The corresponding polarized spectra are shown in Supplementary Fig. S6.

The spontaneous build-up of the circularly polarized radiation at a critical photoexcited density (Fig. 2a) can be quantified by the DoCP ( $\bar{\rho}_c$ ) (Fig. 2c) deduced from the normalized Stokes vector  $s = \{s_1, s_2, s_3\}$  (see Methods). Below threshold, the radiation is unpolarized ( $\bar{\rho}_c \approx 0$ ). Slightly above threshold ( $P_{th} < P < 1.2 P_{th}$ ), the radiation is highly circularly polarized ( $\bar{\rho}_c > 0.95$ ). For  $P > 1.5 P_{th}$ , the radiation becomes elliptically polarized with reduced  $\bar{\rho}_c$ . When the helicity of the circularly polarized pump is switched,  $\bar{\rho}_c$  changes sign but maintains the same magnitude, i.e., the polarization state is symmetric with respect to the helicity of the pump. The pump-flux-dependent DoCP is quantitatively reproduced (dashed lines in Fig. 2c) by a rate-equation model assuming a spin- and density-dependent stimulated pro-

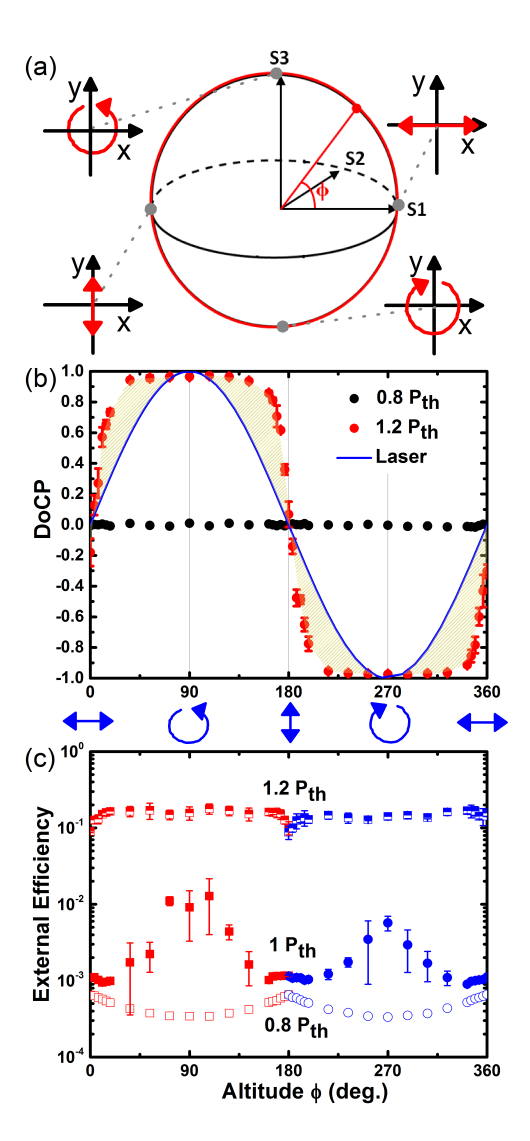


FIG. 3. Spin amplification under an elliptically polarized pump. (a) Representation of polarization states (Stokes vectors) in a Poincaré sphere. The pump polarization is varied along the meridian in the  $s_1$ - $s_3$  (x-z) plane. (b) The time-integrated DoCP ( $\bar{\rho}_c$ ) of the spin-polarized laser radiation as a function of pump DoCP ( $\rho_c^p$ ) (blue line), at 0.8 (black dots), 1.0 (magenta dots) and 1.2  $P_{th}$  (red dots). (c) External quantum efficiency ( $\eta_{ex}$ ) vs. pump DoCP ( $\rho_c^p$ , represented by the altitude  $\phi$ ) at 1.2, 1.0, and 0.8  $P_{th}$ . The pump flux is maintained at a constant when  $\rho_c^p$  is varied. For a specific  $\phi$ , only the  $\eta_{ex}$  of the majority polarized emission component is shown ( $\sigma^+$  for  $0^\circ \leq \phi < 180^\circ$  and  $\sigma^-$  for  $180^\circ \leq \phi < 360^\circ$ ).  $\eta_{ex}$  of the minority component is not shown, owing to a low signal-to-noise ratio for  $\rho_c^p \sim \pm 1$ . Error bars represent the standard deviation of  $\eta_{ex}$  over five measurements.

cess, as described in Supplementary Material. Moreover, under a linearly polarized pump (not shown), elliptically polarized radiation with a finite degree of circular and linear polarization (<0.3) appears only slightly above threshold for  $P_{th} < P < 1.2\,P_{th}$ . The polarization ellipse can be oriented toward the [110] or [1 $\bar{1}0$ ] crystallographic

direction of the GaAs layers, owing to a weak TE-TM mode energy splitting (<50  $\mu$ eV at  $k_{\parallel}=0$ , Supplementary Fig. S1b) induced by an anisotropic crystalline field.

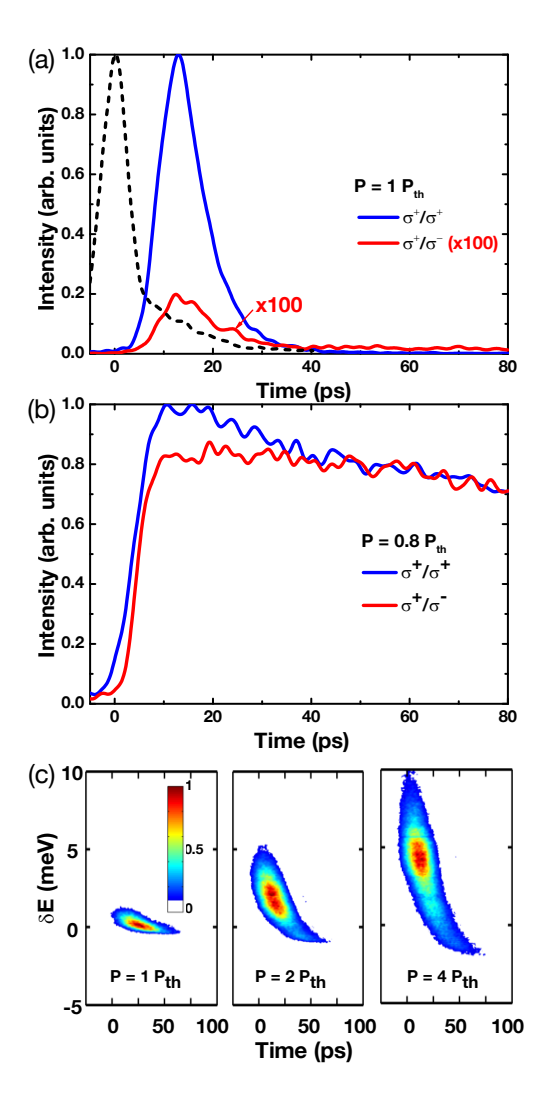


FIG. 4. Dynamics and energy relaxation. (a) Polarized time-dependent luminescence at  $k_{\parallel}=0$  for P=1.0  $P_{th}$  under a circular polarized  $(\sigma^+)$  pump. Blue (red) curves represent the co-circular  $I^+(t)$  [cross-circular  $I^-(t)$ ] components. Note that the cross-circular component shown at  $P_{th}$  is multiplied by a factor of 100. The time zero is determined from the instrument response (black dashed curve), which is measured via pump laser pulses reflected off the sample surface. The time traces are spectrally integrated (temporal resolution  $\approx 5$  ps). (b) Same as (a) but for P=0.8  $P_{th}$ . (c) Temporally and spectrally resolved streak spectral images of the co-circular component  $I^+(\delta E,t)$  at P=1.0, 2.0, and 4.0  $P_{th}$ . The y-axis  $(\delta E)$  is offset with respect to 1.408 eV, the lasing energy at  $P_{th}$ . The temporal resolution is  $\approx 30$  ps owing to the grating-induced dispersion.

Another manifestation of the spin-dependent process is highly circularly polarized lasing even under a nonresonant elliptically polarized optical excitation (Fig. 3). Here, the pump flux transmitted into the microcavity

sample is kept constant with varying pump circular polarization  $(\rho_c^p)$ , represented by the pump Stokes vector tracing a meridian at the Poincaré sphere). When the initial spin-dependent population imbalance is controlled by varying  $\rho_c^p$ , the DoCP of the lasing radiation  $(\bar{\rho}_c)$  can exceed that of the pump for  $1.0 P_{th} < P < 1.5 P_{th}$  (Fig. 3b). Highly circularly polarized lasing ( $\bar{\rho}_c > 0.8$ ) occurs even when  $\rho_c^p$  is as low as 0.5 (altitude  $\phi = 30^\circ$ ). Next, we consider a polarization-dependent external efficiency  $(\eta_{ex}^{\pm})$  (Fig. 3c), defined as the ratio of the polarized emission flux emanating from the front surface (output) to the pump flux transmitted into the microcavity of the same polarization (input). The external efficiency  $\eta_{ex}$  of the majority polarized emission component is less than  $10^{-3}$ below threshold, and increases by two orders of magnitude at 1.2  $P_{th}$ . In both cases,  $\eta_{ex}$  is insensitive to  $\rho_c^p$ . At threshold,  $\eta_{ex}$  exceeds  $10^{-2}$  for  $\rho_c^p \approx 1$  ( $\phi = 90^{\circ}$ ,  $270^{\circ}$ ), while it remains  $\sim 10^{-3}$  for  $\rho_c^p \approx 0$  ( $\phi = 0^{\circ}$ , 180°). The low  $\eta_{ex}$  below threshold is due to significant loss through non-radiative recombination, reabsorption and emissions into other non-lasing modes. With increasing pump flux, a stimulated process dominated over loss, yielding a dramatic increase of  $\eta_{ex}$  above threshold. A competition between loss and spin-dependent stimulation can result in the observed "spin amplification"  $(\bar{\rho_c} > \rho_c^p)$  effect under elliptically polarized pump, which is qualitatively reproduced by the aforementioned model (Supplementary Fig. S8).

To understand the mechanism of the spin-polarized laser action, it is necessary to investigate the polarization dynamics through time-resolved polarimetry and spectroscopy. Fig. 4 shows selected time-resolved co- and cross-circularly polarized luminescence  $[I^{\pm}(t)]$  under a  $\sigma^+$  circularly polarized pump. Below threshold, the timedependent  $\rho_c(t)$  reaches ~0.1 when luminescence reaches its peak, and then decays with a time constant less than 10 ps, as demonstrated by the minimal transient difference between  $I^+(t)$  and  $I^-(t)$  at  $P = 0.8 P_{th}$  (Fig. 4b). At threshold, the co-circular component commences pulsed laser action within 30 ps, while the cross-circular component remains negligible  $[I^+(t)/I^-(t) > 100]$  (Fig. 4a). Such a high  $\rho_c(t) > 0.9$  throughout the pulsed duration is indicative of a spin-dependent stimulated process through which spin polarization is amplified. In contrast, such spin-dependent stimulation does not occur in the absence of cavity. By removing the top DBR mirror layers, we determine  $\rho_c(t)$  to be always less than 0.1 in InGaAs MQWs with similar photoexcited e-h carrier densities (Supplementary Fig. S4).

We further conduct temporally and spectrally resolved measurements, as shown in Fig. 4c. At threshold, the radiation remains spectrally narrow, with a peak energy that is nearly constant with time. Above threshold, the radiation expands spectrally when the laser action commences and gradually redshifts with time. Moreover, polarimetric measurements reveal a circularly polarized high-energy component during the initial 10-20 ps pulsed radiation followed by an unpolarized low-energy one for P>1.5  $P_{th}$  (Supplementary Fig. S7). The co- and cross-circular components have the same transient spectral peak energy depending on the total carrier, indicating a spin-independent chemical potential  $\mu$ .

#### DISCUSSION

We propose that when the chemical potential  $(\mu)$  of the degenerate e-h plasma  $(M_{eh})$  advances toward the cavity resonance  $(E_c)$ , a fraction of the e-h pairs near the Fermi edge can couple effectively to the cavity light field, forming a coherent state  $(n_0)$ . When the conversion from  $M_{eh}$  into  $n_0$  overcomes the decay of  $n_0$ , the occupation number in  $n_0$  approaches unity. Subsequently, a stimulated process  $(\propto M_{eh}n_0)$  prevails, resulting in a nonlinear population increase of  $n_0$  and laser radiation with increasing  $M_{eh}$ . The lasing energy is largely determined by the  $\mu$  of  $M_{eh}$ , which displays substantial energy blueshifts with increasing photoexcited density. On the other hand, the presence of a cavity is necessary to ensure the emergence of correlated e-h pairs near the Fermi edge.

In this microcavity, lasing polarization is determined by  $n_0$  owing to spin-preserved stimulation. The polarization of  $n_0$  can be effectively controlled by optical pumping because of a negligible TE-TM mode energy splitting at  $k_{\parallel} = 0$ . Moreover, the cooling time of nonresonantly photoexcited carriers is comparable to the spin relaxation time  $(\tau_s)$ . Consequently, under a circularly polarized  $\sigma^+$ pump, a sizable spin-imbalanced population is built up when carriers are cooled down to  $M_{eh}$ . In the absence of stimulation (below-threshold), radiation from  $n_0$  is longlived because of a relatively long population decay time of  $M_{eh}$  (~ 100  $\tau_s$ ). Therefore, the time-integrated circular polarization  $\bar{\rho}_c$  is close to zero (unpolarized). In this regime, the non-radiative loss dominates because of an inefficient conversion from  $M_{eh}^{\pm}$  to radiative  $n_0^{\pm}$ . As a result, the overall radiative efficiency of the e-h system is low. When the stimulation condition is satisfied for  $M_{eh}^+$ , but not  $M_{eh}^-$ , the conversion rate from  $M_{eh}^+$  to radiative  $n_0^+$  increases rapidly, yielding a macroscopic population in  $n_0^+$  and a high overall radiative efficiency. In contrast, the overall radiative efficiency for  $n_0^-$  remains minimal. Therefore, the resultant *pulsed* laser radiation is circularly polarized with near unity  $\bar{\rho}_c$ . Such fully circularly polarized lasing only occurs in a limited photoexcited regime, which is determined by the finite spin-imbalance between  $M_{eh}^+$  and  $M_{eh}^-$  when carriers are cooled down. When both  $M_{eh}^+$  and  $M_{eh}^-$  reach the stimulation condition at high photoexcited density, laser radiation display a reduced  $\bar{\rho}_c$ . Temporally, the decreasing  $\mu$  manifests in radiation redshifts, accounting partially to linewidth broadening in time-integrated spectra (Fig. 4c and Fig. 2b). The temporal evolution of  $\mu$  and spin population imbalance also account for an apparent spin-dependent energy splitting of about 1-2 meV (Fig. 2b and Supplementary Fig. S6). Initially, lasing from  $n_0^+$  at high energy dominates because spin-flipping from  $M_{eh}^+$  to  $M_{eh}^-$  is minimal. With increasing time delay, spin-flipping from  $M_{eh}^+$  to  $M_{eh}^+$  becomes significant, and laser radiation from both  $n_0^+$  and  $n_0^-$  appear at lower energy.

In Supplementary Material, we provide a phenomenological rate-equation model including spin-dependent stimulation and loss, which reproduces quantitatively the spin-polarized lasing as a function of photoexcited density and pump polarization. However, a microscopic model including Coulomb many-body effects, such as one based on Maxwell-Bloch equations beyond a phenomenological spin-flip model [17], is necessary to substantiate that hypothesis. It is also important to analyze polarized spectral characteristics and dynamics of lasers with highly interacting carriers in the gain media for further understanding of Coulomb many-body effects [18–22] in high-density coupled *e-h*-photon systems [14, 15].

In principle, the high-density *e-h*-plasma lasing described here can be modeled by a self-consistent numerical analysis developed for conventional semiconductor lasers [23, 24], provided that strong optical nonlinearities induced by Coulomb many-body effects such as screening, bandgap renormalization, and phase-space filling are considered.

The spin-polarized laser studied here has a structure similar to vertical-cavity surface-emitting lasers (VC-SELs) [25] and microcavities used for studies of excitonpolariton condensates [26–34]. We thus wish to compare several spectral characteristics and polarization properties in these systems. Here, spin-polarized lasing occurs in a highly nonresonantly optically excited microcavity at room temperature. Such a spin-polarized laser exhibits nonlinear energy shifts, spin-dependent energy splittings, and linewidth broadening with increasing photoexcited density (Fig. 2 and Supplementary Fig. S6). Interestingly, the spin-polarized lasing spectra of the highly photo excited microcavity resemble the qain those calculated for an e-h plasma at a lower density and sub-100-K effective temperature, when Coulomb many-body effects, including e-h correlation and band-gap renormalization, are considered [35]. In VCSELs, lasing energy is typically determined by the bare cavity resonance and has limited energy shifts [36]. Additionally, amplitude and phase fluctuations induced by modulation of the index of refraction of the gain medium can result in linewidth broadening with increasing carrier density [37]. Polarization properties of VCSELs are typically affected by crystalline anisotropies [38], except for a few spin-controlled lasers [3–6]. On the other hand, exciton-polariton condensates are typically studied in a low photoexcited density below the Mott transition [39] at cryogenic tem-They generally display considerable specperatures. tral blueshifts and broadening with increasing photoexcited density. The spectral shifts are due to polariton-polariton interactions, while the spectral broadening is generally attributed to decoherence and fluctuations induced by interactions [40]. Furthermore, polariton condensates exhibit diverse polarization properties and spin-dependent phenomena depending on materials and excitation conditions [41–50]. Finally, we reiterate that the spin-dependent stimulation and high optical nonlinearities play an important role in facilitating the observed spin-polarized lasing presented here. The ultrafast room-temperature spin-polarized lasing occurs in a highly photoexcited microcavity. Our results should stimulate activities to exploit spin and many-body effects for fundamental studies of light-matter interactions and facilitate developments of spin-dependent optoelectronic devices.

We thank Mark Dykman, Brage Golding, John A. McGuire, Carlo Piermarocchi, Y. Ron Shen, and Hailin Wang for the discussions, and Jack Bass for critical reading of the manuscript. This work was supported by the NSF DMR-0955944.

#### Appendix A: Methods

Sample fabrication. We grow the microcavity on a semi-insulating (100)-GaAs substrate using a molecular beam epitaxy method. A schematic of the structure and a cross-sectional SEM image of the active region are shown in Supplementary Fig. S1. The top (bottom) DBR consists of 17 (20) pairs of GaAs(61-nm)/AlAs (78-nm)  $\lambda/4$  layers. The central cavity layer consists of three stacks of three In<sub>0.15</sub>Ga<sub>0.85</sub>As/GaAs (6-nm/12-nm) quantum wells each, positioned at the anti-nodes of the cavity light field. The structure is entirely undoped and contains a  $\lambda$  GaAs cavity sandwiched by DBRs, resulting in a bare cavity resonance  $E_c \approx 1.41 \text{ eV} (\lambda_c = 880 \text{ nm})$ at room temperature (Supplementary Fig. S2). The QW bandgap  $(E'_q \sim 1.33 \text{ eV})$  is tuned through a rapid thermal annealing process (at 1010-1090°C for 5-10 s), in which the InGaAs QW bandgap blueshifts, owing to the diffusion of gallium ions into the MQW layers. We study samples with  $E'_q \sim$  detuned over a range of about 10-20 meV. All samples display spin-polarized lasing with similar density-dependent polarization properties, spectral shapes and shifts, and dynamics, except for the lasing energy. With increasing photoexcited density, the chemical potential  $\mu$  of e-h plasma can increase up to  $\sim 80 \text{ meV}$ above  $E'_a$ , approaching  $E_c$  (Supplementary Fig. S5). The cavity quality factor Q is about 4000-7000, corresponding to a cavity photon lifetime  $\sim 2$  ps. To investigate the spectral characteristics and spin dynamics InGaAs/GaAs MQWs in the absence of a cavity, we remove top DBR mirror layers by selective wet etching [51].

**Thermal management.** At a high pump flux, the steady-state incident power transmitted to the sample at the 76 MHz repetition rate of the laser would exceed 50

mW, resulting in significant thermal heating and carrier diffusion. The techniques we use to control the thermal heating and diffusion of photoexcited carriers are (1) temporally modulating the pump laser intensity to suppress the thermal carrier heating, and (2) spatially shaping the pump beam profile to enable lasing in a single transverse mode (Supplementary Fig. S3). Steady-state thermal heating can inhibit laser action and lead to spectrally broad redshifted luminescence. To suppress steady-state thermal heating, we temporally modulate the 2-ps 76 MHz pump laser pulse train with a duty cycle (on/off ratio) < 0.5 \%, using a double-pass acousto-optic modulator system [52]. The time-averaged power is limited to below 0.2 mW for all experiments. Multiple transverse modes can simultaneously lase, owing to the diffusion of photoexcited carriers and crystalline disorder, leading to instability and complex lasing characteristics. To control carrier diffusion, we holographically generate a flattop pump beam profile (area  $\approx 300 \ \mu \text{m}^2$ ) at the sample surface, using a spatial beam shaper consisting of a twodimensional (2D) liquid-crystal spatial light modulator (SLM) [53].

Optical excitation. The front surface of the microcavity is positioned at the focal plane of a high-numerical-aperture microscopy objective (N.A. = 0.42, 50×, effective focal length 4 mm). A 3× telescope, a Faraday rotator, a polarizing beam splitter, and the objective form a reflected Fourier transform imaging system (Supplementary Fig. S3). The light fields at the SLM and sample surface form a Fourier transform pair. The 2D SLM (1920 × 1080 pixels, pixel pitch = 8  $\mu$ m) enables us to generate arbitrary pump geometries with a  $\approx 2 \mu$ m spatial resolution at the sample surface using computergenerated phase patterns. The pump flux can be varied by more than two orders of magnitude using a liquid-crystal attenuator.

Imaging spectroscopy. We measure the angular, spectral, and temporal properties of luminescence in the reflection geometry. In a planar microcavity, carriers coupled to the cavity light field are characterized by an in-plane wavenumber  $k_{\parallel} = k \sin(\theta)$ , owing to the twodimensional confinement of both photons and carriers. The leakage photons can thus be used for a direct measurement of the angular distribution of optically active carriers. Angle-resolved luminescence images and spectra are measured through a Fourier transform optical system (Supplementary Fig. S3). A removable f = 200mm lens enables the projection of either the k-space or r-space luminescence on to the entrance plane or slit of the spectrometer. Luminescence is collected through the objective, separated from the reflected specular and scattered pump laser light with a notch filter, and then directed to an imaging spectrometer. A single circular transverse lasing mode with a spatial mode diameter  $\approx 8$  $\mu$ m is isolated for measurements through a pinhole positioned at the conjugate image plane of the microcavity

sample surface. The spectral resolution is  $\approx 0.1$  nm (150  $\mu eV$ ), determined by the dispersion of the grating (1200 grooves/mm) and the entrance slit width (100-200  $\mu m$ ). The spatial (angular) resolution is  $\approx 0.3~\mu m$  (6 mrad) per CCD pixel.

Polarization control and notation. The polarization state of the pump (luminescence) is controlled (analyzed) by a combination of liquid crystal devices, such as variable retarders and polarization rotators, and Glan-Taylor/Glan-Thomson polarizers without mechanical moving parts. A polarization compensator (Berek's variable wave plates) is used to compensate for the phase retardance induced by the reflection from the miniature gold mirror surface. The circularly polarized pump or luminescence with angular momentum  $+\hbar$   $(-\hbar)$  along the pump laser wavevector  $\hat{k} \parallel \hat{z}$  is defined as  $\sigma^+$  ( $\sigma^-$ ). Linearly polarized light with horizontal (vertical) polarization is defined as  $\sigma^X$  ( $\sigma^Y$ ). The polarization state is characterized by the Stokes vector  $\{S_0, S_1, S_2, S_3\}$ .  $S_0$  is the flux and is determined as  $S_0 = I^+ + I^- = I^X + I^Y =$  $I^{45^{\circ}} + I^{135^{\circ}}$ . The Stokes vector can be normalized by its flux  $S_0$  to the Stokes three-vector  $s = \{s_1, s_2, s_3\}$ .  $s_1 = (I^X - I^Y)/(I^X + I^Y)$ ,  $s_2 = (I^{45^\circ} - I^{135^\circ})/(I^{45^\circ} + I^{135^\circ})$ , and  $s_3 = (I^+ - I^-)/(I^+ + I^-)$ .  $I^+$ ,  $I^-$ ,  $I^X$ ,  $I^Y$ ,  $I^{45^\circ}$ , and  $I^{135^\circ}$  are measured time-integrated or temporal intensities of the circular or linear polarized components. We represent the polarization state using the following three quantities: the degree of circular polarization ( $DoCP \equiv \rho_c = s_3$ ), degree of linear polarization ( $DoLP \equiv \rho_l = \sqrt{s_1^2 + s_2^2}$ ), and degree of polarization  $(DoP \equiv \rho = \sqrt{s_1^2 + s_2^2 + s_3^2})$ . The accuracy of the measured polarization state is  $\approx 1-2\%$ .

- \* These authors contributed equally to this work.

  † cwlai@msu.edu
- J. P. Riehl and F. S. Richardson, "Circularly polarized luminescence spectroscopy," Chem Rev 86, 1–16 (1986);
   G. Böhm, R. Muhr, and R. Jaenicke, "Quantitative analysis of protein far UV circular dichroism spectra by neural networks," Protein Eng. 5, 191–195 (1992).
- [2] I. Žutić, J. Fabian, and S. Das Sarma, "Spintronics: Fundamentals and applications," Rev. Mod. Phys. 76, 323–410 (2004); M. I. Dyakonov, ed., Spin Physics in Semiconductors, Springer Series in Solid-State Science, Vol. 157 (Springer, 2008); D. D. Awschalom, L. C. Bassett, A. S. Dzurak, E. L. Hu, and J. R. Petta, "Quantum spintronics: engineering and manipulating atom-like spins in semiconductors." Science 339, 1174–9 (2013).
- [3] H. Ando, T. Sogawa, and H. Gotoh, "Photon-spin controlled lasing oscillation in surface-emitting lasers," Appl. Phys. Lett. 73, 566-568 (1998); J. Rudolph, D. Hägele, H. M. Gibbs, G. Khitrova, and M. Oestreich, "Laser threshold reduction in a spintronic device," Appl. Phys. Lett. 82, 4516-4518 (2003); M. Holub, J. Shin, D. Saha, and P. Bhattacharya, "Electrical spin injection and threshold reduction in a semiconductor laser," Phys.

- Rev. Lett. 98, 146603 (2007); S. Iba, S. Koh, K. Ikeda, and H. Kawaguchi, "Room temperature circularly polarized lasing in an optically spin injected vertical-cavity surface-emitting laser with (110) GaAs quantum wells," Appl. Phys. Lett. 98, 081113 (2011).
- [4] E. L. Blansett, M. G. Raymer, Guoqiang Cui, G. Khitrova, H. M. Gibbs, D. K. Serkland, A. A. Allerman, and K. M. Geib, "Picosecond polarization dynamics and noise in pulsed vertical-cavity surface-emitting lasers," IEEE J. Quantum Electron. 41, 287–301 (2005).
- [5] I. Zutic, R. Oszwaldowski, J. Lee, and C. Gothgen, "Semiconductor spin-lasers," in *Handbook of Spin Transport and Magnetism* (CRC, 2011) pp. 731–745.
- [6] N. C. Gerhardt and M. R. R. Hofmann, "Spin-controlled vertical-cavity surface-emitting lasers," Adv. Opt. Technol. 2012, 268949 (2012); N. Gerhardt, S. Hovel, M. Hofmann, J. Yang, D. Reuter, and A. Wieck, "Enhancement of spin information with vertical cavity surface emitting lasers," Electronics Letters 42, 88–89 (2006); C. Gøthgen, R. Oszwałdowski, A. Petrou, and I. Žutić, "Analytical model of spin-polarized semiconductor lasers," Appl. Phys. Lett. 93, 042513–042513–3 (2008).
- [7] F. Meier and B. P. Zakharchenya, "Optical orientation," (Elsevier, 1984); M. I. Dyakonov and V. I. Perel, "Theory of optical spin orientation of electrons and nuclei in semiconductors," in *Optical Orientation*, Vol. 8 (Elsevier, 1984) pp. 11–72.
- [8] R. Fiederling, M. Keim, G. Reuscher, W. Ossau, G. Schmidt, A. Waag, and L. W. W. Molenkamp, "Injection and detection of a spin-polarized current in a light-emitting diode," Nature 402, 787–790 (1999); Y. Ohno, D. K. Young, B. al Beschoten, F. Matsukura, H. Ohno, and D. D. Awschalom, "Electrical spin injection in a ferromagnetic semiconductor heterostructure," Nature 402, 790–792 (1999).
- [9] M. S. Bresler, O. B. Gusev, and I. A. Merkulov, "Optical orientation of an electron-photon system under conditions of stimulated luminescence," Sov. Phys. JETP 66, 1179 (1987).
- [10] D. Chemla, D. Miller, P. Smith, A. Gossard, and W. Wiegmann, "Room temperature excitonic nonlinear absorption and refraction in gaas/algaas multiple quantum well structures," IEEE J. Quantum Electron. 20, 265–275 (1984); W. H. Knox, R. L. Fork, M. C. Downer, D. A. B. Miller, D. S. Chemla, C. V. Shank, A. C. Gossard, and W. Wiegmann, "Femtosecond dynamics of resonantly excited excitons in roomtemperature GaAs quantum wells," Phys. Rev. Lett. 54, 1306–1309 (1985); D. S. Chemla and D. A. B. Miller, "Room-temperature excitonic nonlinear-optical effects in semiconductor quantum-well structures," J. Opt. Soc. Am. B 2, 1155–1173 (1985); M. Colocci, M. Gurioli, and A. Vinattieri, "Thermal ionization of excitons in GaAs/AlGaAs quantum well structures," J. Appl. Phys. **68**, 2809–2812 (1990).
- [11] J.-H. Kim, G. T. N. II, S. A. McGill, Y. Wang, A. K. Wójcik, A. A. Belyanin, and J. Kono, "Fermi-edge superfluorescence from a quantum-degenerate electron-hole gas," Sci. Rep. 3, 3283 (2013).
- [12] S. Smolka, W. Wuester, F. Haupt, S. Faelt, W. Wegscheider, and A. Imamoglu, "Cavity quantum electrodynamics with many-body states of a two-dimensional electron gas," Science 346, 1258595 (2014); A. Gabbay,

- Y. Preezant, E. Cohen, B. M. Ashkinadze, and L. N. Pfeiffer, "Fermi edge polaritons in a microcavity containing a high density two-dimensional electron gas," Phys. Rev. Lett. **99**, 157402 (2007).
- [13] P. Plochocka-Polack, J. G. Groshaus, M. Rappaport, V. Umansky, Y. Gallais, A. Pinczuk, and I. Bar-Joseph, "Fermi-edge singularity of spin-polarized electrons," Phys. Rev. Lett. 98, 186810 (2007).
- [14] J. Keeling, P. R. Eastham, M. H. Szymanska, and P. B. Littlewood, "BCS-BEC crossover in a system of microcavity polaritons," Phys. Rev. B 72, 115320 (2005).
- [15] K. Kamide and T. Ogawa, "What determines the wave function of electron-hole pairs in polariton condensates?" Phys. Rev. Lett. 105, 056401 (2010); "Ground-state properties of microcavity polariton condensates at arbitrary excitation density," Phys. Rev. B 83, 165319 (2011); M. Yamaguchi, K. Kamide, T. Ogawa, and Y. Yamamoto, "BEC-BCS-laser crossover in Coulomb-correlated electron-hole-photon systems," New J. Phys. 14, 065001 (2012); M. Yamaguchi, K. Kamide, R. Nii, T. Ogawa, and Y. Yamamoto, "Second thresholds in BEC-BCS-laser crossover of exciton-polariton systems," Phys. Rev. Lett. 111, 026404 (2013).
- [16] A. T. Friberg and R. J. Sudol, "Propagation parameters of gaussian Schell-model beams," Opt. Commun. 41, 383 – 387 (1982).
- [17] M. San Miguel, Q. Feng, and J. V. Moloney, "Light-polarization dynamics in surface-emitting semiconductor lasers," Phys. Rev. A 52, 1728–1739 (1995); J. Martin-Regalado, F. Prati, M. San Miguel, and N. B. Abraham, "Polarization properties of vertical-cavity surface-emitting lasers," IEEE J. Quantum Electron. 33, 765–783 (1997); M. P. van Exter, R. F. M. Hendriks, and J. P. Woerdman, "Physical insight into the polarization dynamics of semiconductor vertical-cavity lasers," Phys. Rev. A 57, 2080–2090 (1998).
- [18] H. Noyes, "New nonsingular integral equation for two-particle scattering," Phys. Rev. Lett. 15, 538-540 (1965);
  G. D. Mahan, "Excitons in degenerate semiconductors," Phys. Rev. 153, 882-889 (1967).
- [19] C. Comte and P. Nozières, "Exciton Bose condensation: the ground state of an electron-hole gas I. Mean field description of a simplified model," J. Phys.-Paris 43, 1069–1081 (1982); P. Nozières and C. Comte, "Exciton Bose condensation: the ground state of an electron-hole gas II. Spin states, screening and band structure effects," J. Phys.-Paris 43, 1083–1098 (1982).
- [20] P. Nozières and S. Schmitt-Rink, "Bose condensation in an attractive fermion gas: From weak to strong coupling superconductivity," J. Low Temp. Phys. 59, 195– 211 (1985).
- [21] S. Schmitt-Rink and C. Ell, "Excitons and electron-hole plasma in quasi-two-dimensional systems," J. Lumin. 30, 585 – 596 (1985); S. Schmitt-Rink, D. S. Chemla, and D. A. B. Miller, "Theory of transient excitonic optical nonlinearities in semiconductor quantum-well structures," Phys. Rev. B 32, 6601–6609 (1985).
- [22] F. Jahnke and S. W. Koch, "Many-body theory for semi-conductor microcavity lasers," Phys. Rev. A 52, 1712–1727 (1995); M. Kira, F. Jahnke, S. W. Koch, J. D. Berger, D. V. Wick, T. R. Nelson, G. Khitrova, and H. M. Gibbs, "Quantum theory of nonlinear semiconductor microcavity luminescence explaining "Boser" experiments," Phys. Rev. Lett. 79, 5170–5173 (1997); M. Kira

- and S. W. Koch, "Many-body correlations and excitonic effects in semiconductor spectroscopy," Prog. Quantum Electron. **30**, 155–296 (2006); S. W. Koch, M. Kira, G. Khitrova, and H. M. Gibbs, "Semiconductor excitons in new light," Nature Mater. **5**, 523–531 (2006).
- [23] S. W. Koch, F. Jahnke, and W. W. Chow, "Physics of semiconductor microcavity lasers," Semicond. Sci. Technol. 10, 739 (1995).
- [24] R. Sarzala, T. Czyszanowski, M. Wasiak, M. Dems, L. Piskorski, W. Nakwaski, and K. Panajotov, "Numerical self-consistent analysis of VCSELs," Adv. Opt. Technol. 2012, 17 (2012); P. Debernardi, "Three-dimensional modeling of VCSELs," in VCSELs (Springer Berlin Heidelberg, 2013) pp. 77–117.
- [25] K. Iga, F. Koyama, and S. Kinoshita, "Surface emitting semiconductor lasers," IEEE J. Quantum Electron. 24, 1845–1855 (1988); R. Michalzik, ed., "VCSELs: A research review," in VCSELs, Springer Series in Optical Sciences, Vol. 166 (Springer, 2013) pp. 3–18.
- [26] H. Deng, G. Weihs, C. Santori, J. Bloch, and Y. Yamamoto, "Condensation of semiconductor microcavity exciton polaritons," Science 298, 199–202 (2002).
- [27] J. Kasprzak, M. Richard, S. Kundermann, A. Baas, P. Jeambrun, J. M. J. Keeling, F. M. Marchetti, M. H. Szymańska, R. André, J. L. Staehli, V. Savona, P. B. Littlewood, B. Deveaud-Plédran, and L. S. Dang, "Bose-Einstein condensation of exciton polaritons," Nature 443, 409–414 (2006).
- [28] R. Balili, V. Hartwell, D. Snoke, L. Pfeiffer, and K. West, "Bose-Einstein condensation of microcavity polaritons in a trap," Science **316**, 1007–1010 (2007).
- [29] C. W. Lai, N. Y. Kim, S. Utsunomiya, G. Roumpos, H. Deng, M. D. Fraser, T. Byrnes, P. Recher, N. Kumada, T. Fujisawa, and Y. Yamamoto, "Coherent zero-state and π-state in an exciton-polariton condensate array." Nature 450, 529–32 (2007); S. Utsunomiya, L. Tian, G. Roumpos, C. W. Lai, N. Kumada, T. Fujisawa, M. Kuwata-Gonokami, A. Löffler, S. Höfling, a. Forchel, and Y. Yamamoto, "Observation of Bogoliubov excitations in exciton-polariton condensates," Nature Phys. 4, 700–705 (2008).
- [30] K. G. Lagoudakis, M. Wouters, M. Richard, A. Baas, I. Carusotto, R. André, L. S. Dang, and B. Deveaud-Plédran, "Quantized vortices in an excitonpolariton condensate," Nature Phys. 4, 706–710 (2008); Lagoudakis, T. Ostatnický, A. V. Kavokin, Y. G. Rubo, R. André, and B. Deveaud-Plédran, "Observation of half-quantum vortices in an exciton-polariton condensate," Science **326**, 974–976 (2009); D. Sanvitto, F. M. Marchetti, M. H. Szymańska, G. Tosi, M. Baudisch, F. P. Laussy, D. N. Krizhanovskii, M. S. Skolnick, L. Marrucci, A. Lemaître, J. Bloch, C. Tejedor, and L. Viña, "Persistent currents and quantized vortices in a polariton superfluid," Nature Phys. 6, 527–533 (2010); G. Nardin, G. Grosso, Y. Léger, B. Pietka, F. Morier-Genoud, and B. Deveaud-Plédran, "Hydrodynamic nucleation of quantized vortex pairs in a polariton quantum fluid," Nature Phys. 7, 635–641 (2011); G. Roumpos, M. D. Fraser, A. Löffler, S. Höfling, A. Forchel, and Y. Yamamoto, "Single vortex-antivortex pair in an exciton-polariton condensate," Nature Phys. 7, 129–133 (2011).
- [31] D. Bajoni, P. Senellart, A. Lemaitre, and J. Bloch, "Photon lasing in GaAs microcavity: Similarities with a polariton condensate," Phys. Rev. B 76, 201305 (2007);

- D. Bajoni, P. Senellart, E. Wertz, I. Sagnes, A. Miard, A. Lemaître, and J. Bloch, "Polariton laser using single micropillar GaAs-GaAlAs semiconductor cavities," Phys. Rev. Lett. 100, 047401 (2008); M. Assmann, J.-S. S. Tempel, F. Veit, M. Bayer, A. Rahimi-Iman, A. Löffler, S. Höfling, S. Reitzenstein, L. Worschech, and A. Forchel, "From polariton condensates to highly photonic quantum degenerate states of bosonic matter." Proc. Nat. Acad. Sci. 108, 1804–9 (2011); E. Kammann, H. Ohadi, M. Maragkou, A. V. Kavokin, and P. G. Lagoudakis, "Crossover from photon to exciton-polariton lasing," New J. Phys. 14, 105003 (2012).
- [32] G. Christmann and J. J. Baumberg, "The future prospects of room-temperature polariton lasers," in *Exciton Polaritons in Microcavities* (Springer, 2012) pp. 329–348
- [33] C. Schneider, A. Rahimi-Iman, N. Y. Kim, J. Fischer, I. G. Savenko, M. Amthor, M. Lermer, A. Wolf, L. Worschech, V. D. Kulakovskii, I. A. Shelykh, M. Kamp, S. Reitzenstein, A. Forchel, Y. Yamamoto, and S. Höfling, "An electrically pumped polariton laser," Nature 497, 348–352 (2013); Pallab Bhattacharya, Bo Xiao, Ayan Das, Sishir Bhowmick, and Junseok Heo, "Solid state electrically injected exciton-polariton laser," Phys. Rev. Lett. 110, 206403 (2013).
- [34] H. Deng, H. Haug, and Y. Yamamoto, "Exciton-polariton Bose-Einstein condensation," Rev. Mod. Phys. 82, 1489–1537 (2010); J. Keeling and Natalia Berloff, "Exciton-polariton condensation," Contemp. Phys. 52, 131–151 (2011); B. Deveaud-Plédran, "On the condensation of polaritons," J. Opt. Soc. Am. B 29, A138–A145 (2012); I. Carusotto and C. Ciuti, "Quantum fluids of light," Rev. Mod. Phys. 85, 299–366 (2013); J. Bloch, "Polariton condensates in low dimensional cavities," in Physics of Quantum Fluids (Springer, 2013) pp. 177–199; T. Byrnes, N. Y. Kim, and Y. Yamamoto, "Exciton-polariton condensates," Nature Phys. 10, 803–813 (2014).
- [35] S. Schmitt-Rink, C. Ell, and H. Haug, "Many-body effects in the absorption, gain, and luminescence spectra of semiconductor quantum-well structures," Phys. Rev. B 33, 1183–1189 (1986).
- [36] C. J. Chang-Hasnain, "Tunable VCSEL," IEEE J.
   Sel. Topics Quantum Electron. 6, 978–987 (2000);
   F. Koyama, "Recent advances of VCSEL photonics," J.
   Lightw. Technol. 24, 4502–4513 (2006).
- [37] C. H. Henry, "Theory of the linewidth of semiconductor lasers," IEEE J. Quantum Electron. 18, 259–264 (1982); "Phase noise in semiconductor lasers," J. Lightwave Technol. 4, 298–311 (1986); Y. Arakawa and A. Yariv, "Theory of gain, modulation response, and spectral linewidth in AlGaAs quantum well lasers," IEEE J. Quantum Electron. 21, 1666–1674 (1985).
- [38] K. Panajotov and F. Prati, "Polarization dynamics of VCSELs," in VCSELs (Springer, 2013) pp. 181–231;
   J. M. M. Ostermann and R. Michalzik, "Polarization control of VCSELs," in VCSELs, Springer Series in Optical Sciences, Vol. 166 (Springer, 2013) pp. 147–179.
- [39] G. Manzke, D. Semkat, and H. Stolz, "Mott transition of excitons in GaAs-GaAlAs quantum wells," New J. Phys. 14, 095002 (2012); L. Kappei, J. Szczytko, F. Morier-Genoud, and B. Deveaud, "Direct observation of the Mott transition in an optically excited semiconductor quantum well," Phys. Rev. Lett. 94, 147403

- (2005); C. F. Klingshirn, "The intermediate density regime," in *Semiconductor Optics* (Springer, 2012) pp. 507–560; "The electron-hole plasma," in *Semiconductor Optics* (Springer, 2012) pp. 561–597; "Stimulated emission and laser processes," in *Semiconductor Optics* (Springer, 2012) Chap. 22, pp. 599–622.
- [40] M. Wouters, I. Carusotto, and C. Ciuti, "Spatial and spectral shape of inhomogeneous nonequilibrium exciton-polariton condensates," Phys. Rev. B 77, 115340 (2008);
  P. Schwendimann and A. Quattropani, "Statistics of the polariton condensate," Phys. Rev. B 77, 085317 (2008);
  H. Haug, H. T. Cao, and D. B. Tran Thoai, "Coherence and decoherence of a polariton condensate," Phys. Rev. B 81, 245309 (2010);
  H. Haug, T. D. Doan, H. T. Cao, and D. B. Tran Thoai, "Temporal first- and second-order correlations in a polariton condensate," Phys. Rev. B 85, 205310 (2012).
- [41] M. D. Martín, G. Aichmayr, L. Viña, and R. André, "Polarization control of the nonlinear emission of semiconductor microcavities," Phys. Rev. Lett. 89, 077402 (2002).
- [42] H. Deng, G. Weihs, D. Snoke, J. Bloch, and Y. Yamamoto, "Polariton lasing vs. photon lasing in a semi-conductor microcavity," Proc. Natl. Acad. Sci. U.S.A. 100, 15318–15323 (2003); I. A. Shelykh, K. V. Kavokin, A. V. Kavokin, G. Malpuech, P. Bigenwald, H. Deng, G. Weihs, and Y. Yamamoto, "Semiconductor microcavity as a spin-dependent optoelectronic device," Phys. Rev. B 70, 035320 (2004); H. T. Cao, T. D. Doan, D. B. Tran Thoai, and H. Haug, "Polarization kinetics of semiconductor microcavities investigated with a Boltzman approach," Phys. Rev. B 77, 075320 (2008).
- [43] D. Ballarini, A. Amo, L. Viña, D. Sanvitto, M. S. Skolnick, and J. S. Roberts, "Transition from the strong-to-the weak-coupling regime in semiconductor microcavities: Polarization dependence," Appl. Phys. Lett. 90, 201905 (2007).
- [44] J. J. Baumberg, A. V. Kavokin, S. Christopoulos, A. J. D. Grundy, R. Butté, G. Christmann, D. D. Solnyshkov, G. Malpuech, G. Baldassarri Höger von Högersthal, E. Feltin, J. F Carlin, and N. Grandjean, "Spontaneous polarization buildup in a room-temperature polariton laser," Phys. Rev. Lett. 101, 136409 (2008); H. Ohadi, E. Kammann, T. C. H. Liew, K. G. Lagoudakis, A. V. Kavokin, and P. G. Lagoudakis, "Spontaneous symmetry breaking in a polariton and photon laser," Phys. Rev. Lett. 109, 016404 (2012).
- [45] L. Viña, L. Munoz, E. Perez, J. Fernandez-Rossier, C. Tejedor, and K. Ploog, "Spin splitting in a polarized quasi-two-dimensional exciton gas," Phys. Rev. B **54**, R8317–R8320 (1996); L. Viña, "Spin relaxation in low-dimensional systems," J. Phys.: Condens. Matter 11, 5929 (1999); C. Ciuti, V. Savona, C. Piermarocchi, A. Quattropani, and P. Schwendimann, "Role of the exchange of carriers in elastic exciton-exciton scattering in quantum wells," Phys. Rev. B 58, 7926-7933 (1998); S. Ben-Tabou de-Leon and B. Laikhtman, "Mott transition, biexciton crossover, and spin ordering in the exciton gas in quantum wells," Phys. Rev. B 67, 235315 (2003); M. Vladimirova, S. Cronenberger, D. Scalbert, K. V. Kavokin, A. Miard, A. Lemaître, J. Bloch, D. Solnyshkov, G. Malpuech, and A. V. Kavokin, "Polariton-polariton interaction constants in microcavities," Phys. Rev. B 82, 075301 (2010); T. Lecomte, D. Taj, A. Lemaître,

- J. Bloch, C. Delalande, J. Tignon, and P. Roussignol, "Polariton-polariton interaction potentials determination by pump-probe degenerate scattering in a multiple microcavity," Phys. Rev. B 89, 155308 (2014); M. Sich, F. Fras, J. K. Chana, M. S. Skolnick, D. N. Krizhanovskii, A. V. Gorbach, R. Hartley, D. V. Skryabin, S. S. Gavrilov, E. A. Cerda-Méndez, K. Biermann, R. Hey, and P. V. Santos, "Effects of spin-dependent interactions on polarization of bright polariton solitons," Phys. Rev. Lett. 112, 046403 (2014); N. Takemura, S. Trebaol, M. Wouters, M. T. . T. Portella-Oberli, and B. Deveaud, "Polaritonic Feshbach resonance," Nature Phys. 10, 500–504 (2014).
- [46] E. Kammann, T. C. H. Liew, H. Ohadi, P. Cilibrizzi, P. Tsotsis, Z. Hatzopoulos, P. G. Savvidis, A. V. Kavokin, and P. G. Lagoudakis, "Nonlinear optical spin Hall effect and long-range spin transport in polariton lasers," Phys. Rev. Lett. 109, 036404 (2012); A. V. Sekretenko, S. S. Gavrilov, S. I. Novikov, V. D. Kulakovskii, S. Höfling, C. Schneider, M. Kamp, and A. Forchel, "Spin and density patterns of polariton condensates resonantly excited in strained planar microcavities with a nonuniform potential landscape," Phys. Rev. B 88, 205302 (2013).
- [47] R. Cerna, Y. Léger, T. K. Paraïso, M. Wouters, F. Morier-Genoud, M. T. Portella-Oberli, and B. Deveaud, "Ultrafast tristable spin memory of a coherent polariton gas." Nature Commun. 4, 2008 (2013); F. Manni, Y. Léger, Y. G. Rubo, R. André, and B. Deveaud, "Hyperbolic spin vortices and textures in exciton-polariton condensates," Nature Commun. 4, 2590 (2013); M. Wouters, T. K. Paraïso, Y. Léger, R. Cerna, F. Morier-Genoud, M. T. Portella-Oberli, and B. Deveaud-Plédran, "Influence of a nonradiative reservoir on polariton spin multistability," Phys. Rev. B 87, 045303 (2013).
- [48] J. Fischer, S. Brodbeck, A. V. Chernenko, I. Lederer, A. Rahimi-Iman, M. Amthor, V. D. Kulakovskii, L. Worschech, M. Kamp, M. Durnev, C. Schneider, A.V. Kavokin, and S. Höfling, "Anomalies of a nonequilibrium spinor polariton condensate in a magnetic field," Phys. Rev. Lett. 112, 093902 (2014).
- [49] K. V. Kavokin, I. A. Shelykh, A. V. Kavokin, G. Malpuech, and P. Bigenwald, "Quantum theory of spin dynamics of exciton-polaritons in microcavities," Phys. Rev. Lett. 92, 017401 (2004); I. A. Shelykh, Yuri G. Rubo, G. Malpuech, D. D. Solnyshkov, and A. Kavokin, "Polarization and propagation of polariton condensates," Phys. Rev. Lett. 97, 066402 (2006); I. A. Shelykh, A. V. Kavokin, Y. G. Rubo, T. C. H. Liew, and G. Malpuech, "Polariton polarization-sensitive phenomena in planar semiconductor microcavities," Semicond. Sci. Technol. 25, 013001 (2010).
- [50] A. Kavokin, "Spin effects in exciton-polariton condensates," in Exciton Polaritons in Microcavities (Springer, 2012) pp. 233–244; "Bosonic spin transport," in Physics of Quantum Fluids (Springer, 2013) pp. 39–50; Y. G. Rubo, "Mean-field description of multicomponent exciton-polariton superfluids," in Physics of Quantum Fluids (Springer, 2013) pp. 51–70; H. Flayac, D. D. Solnyshkov, and G. Malpuech, "Spin effects in polariton condensates: From half-solitons to analogues of wormholes," in Physics of Quantum Fluids (Springer, 2013) pp. 71–98.
- [51] G. C. DeSalvo, W. F. Tseng, and J. Comas, "Etch

- rates and selectivities of citric acid/hydrogen peroxide on GaAs, Al<sub>0.3</sub>Ga<sub>0.7</sub>As, In<sub>0.2</sub>Ga<sub>0.8</sub>As, In<sub>0.53</sub>Ga<sub>0.47</sub>As, In<sub>0.52</sub>Al<sub>0.48</sub>As, and InP," J. Electrochem. Soc. **139**, 831–835 (1992); E. A. Moon, J. L. Lee, and H. M. Yoo, "Selective wet etching of GaAs on AlGaAs for AlGaAs/InGaAs/AlGaAs pseudomorphic high electron mobility transistor," J. Appl. Phys. **84**, 3933 (1998).
- [52] E. A. Donley, T. P. Heavner, F. Levi, M. O. Tataw, and S. R. Jefferts, "Double-pass acousto-optic modulator system," Rev. Sci. Instrum. 76, 063112-063112-6 (2005).
- [53] L. A. Romero and F. M. Dickey, "Lossless laser beam shaping," J. Opt. Soc. Am. A 13, 751–760 (1996).

# Supplementary Material for Spin-polarized lasing in a highly excited semiconductor microcavity

Feng-kuo Hsu, 1, \* Wei Xie, 1, \* Yi-Shan Lee, 2 Sheng-Di Lin, 2 and Chih-Wei Lai 1, †

<sup>&</sup>lt;sup>1</sup>Department of Physics and Astronomy, Michigan State University, East Lansing, MI 48824, USA <sup>2</sup>Department of Electronics Engineering, National Chiao Tung University, Hsinchu 30010, Taiwan

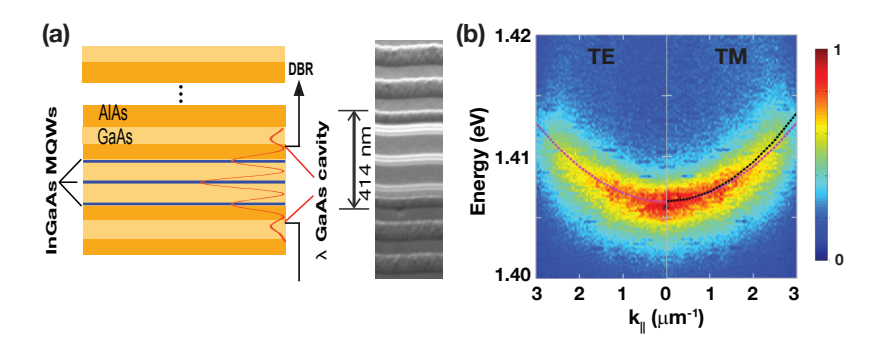


Fig. S1. Microcavity structure and energy splitting of TE-TM modes. (a) Schematic of the microcavity structure: InGaAs multiple quantum wells (MQWs) embedded within a  $\lambda$  (wavelength) GaAs cavity, which has a ~400-nm thick GaAs cavity spacer layer. We adjust the antinodes of the cavity light field to the MQW layers by adding two transitional AlAs layers and a GaAs cap layer. Right sub-figure is cross-sectional scanning electron microscope (SEM) image of microcavity sample. (b) E vs.  $k_{\parallel}$  dispersions for the TE (left) and TM (right) modes under a circularly polarized pump at 1.579 eV and P=0.6  $P_{th}$ . The simulated TE and TM dispersions are shown as magenta and black curves, respectively. The TE-TM energy splitting is less than 50  $\mu$ eV at  $k_{\parallel}=0$ , allowing for effective control of the lasing polarization by optical pumping.

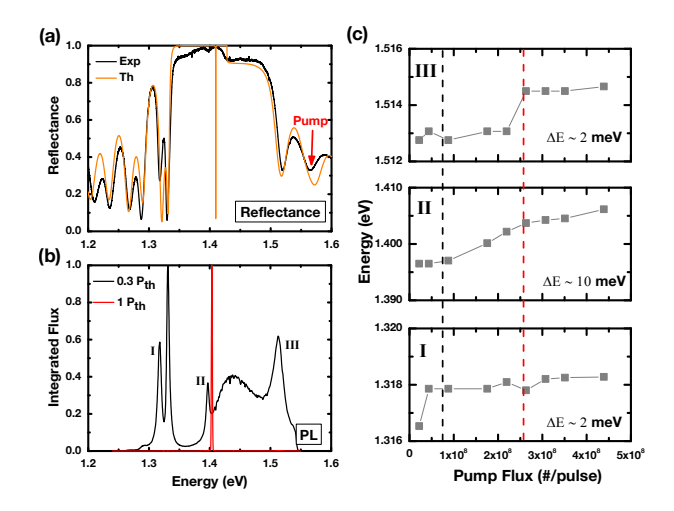


Fig. S2. Reflectance and laser spectral characteristics. (a) Reflectance spectrum at  $k_{\parallel}=0$  from the front surface of a microcavity sample with 1.405 eV lasing energy at threshold: measured (black solid line) and simulated (orange solid line). This sample is an as-grown sample not subject to a rapid thermal annealing process. The simulation is performed via a transfer matrix method, including the optical absorption in GaAs layers, but excluding exciton effects. The cavity resonance ( $E_c$ ) is about 1.41 eV. (b) Emission spectra at  $k_{\parallel}=0$  at at pump P=0.3 and 1.0  $P_{th}$ . Above threshold, luminescence is dominated by the lasing mode (red curve). (c) Spectral peak energy as a function of pump flux (photoexcited density) for emission peaks I, II, and III as indicated in (b). The vertical black and red dashed lines indicate P=0.3 and 1.0  $P_{th}$ , respectively. Emission peak-I and peak-III correspond to a reflection minimum with energy below and above the reflection stop band, while peak-II is near the cavity resonance. Peak-I and peak-III experience less than 2 meV spectral shifts with increasing pump flux. In contrast, peak-II blueshifts more than 10 meV for the same density range, suggesting a strong optical nonlinearity induced by the coupling between the high-density e-h plasma and the cavity light field.

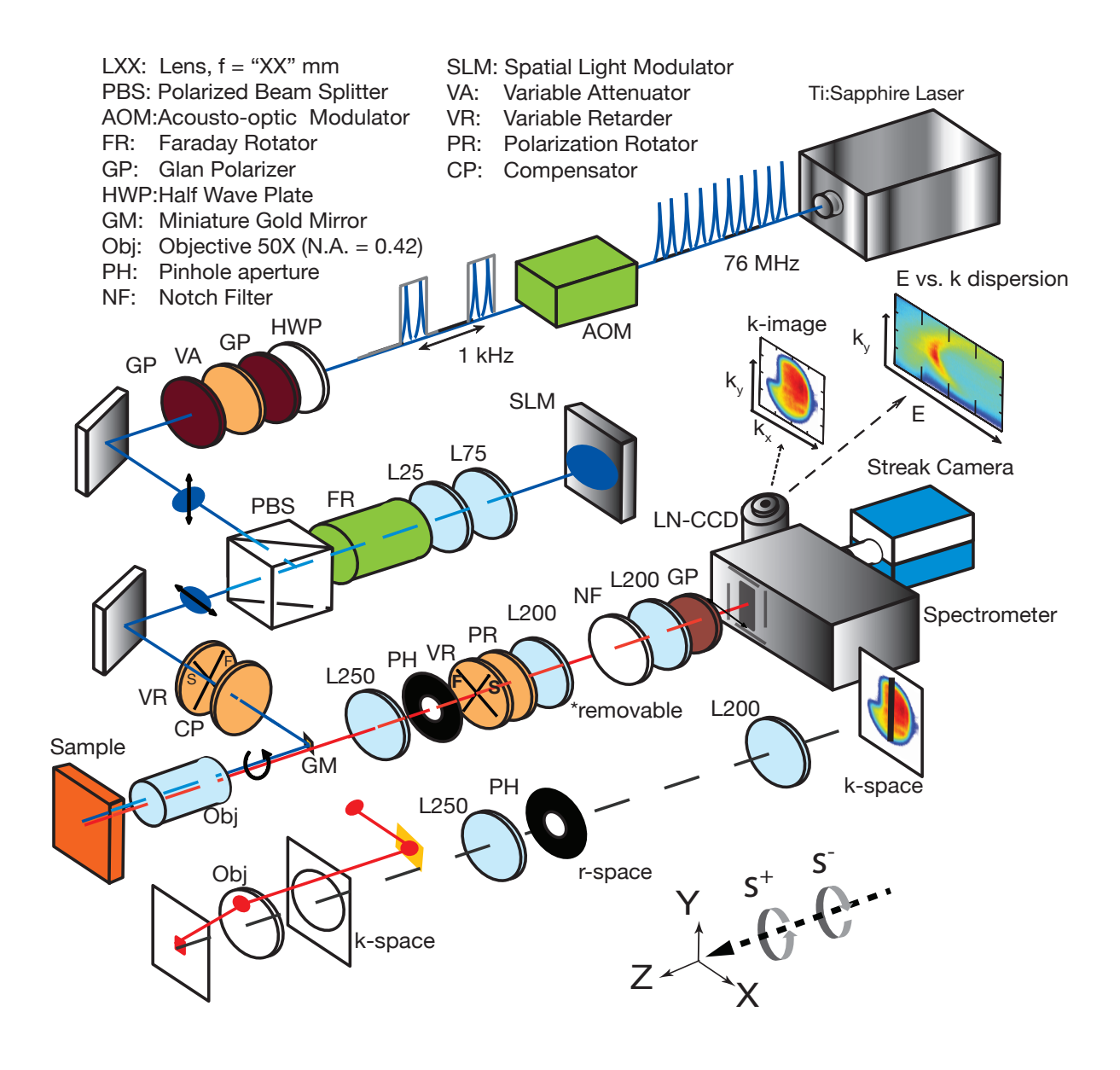


Fig. S3. Experimental set-up: angle-resolved spectroscopy and polarimetry. Luminescence from the microcavity is collected by a microscope objective (N.A. = 0.42, effective focal length  $f_0 = 4$  mm). The collection angle is up to  $\theta \approx 25^{\circ}$  in air. The luminescence with field distribution F(X,Y) is Fourier transformed into a far-field image in the back focal plane of the objective with coordinates  $(u,v) = (f_o \times \sin(\theta_X), f_o \times \sin(\theta_Y))$ . This plane is mapped into k-space with  $(k_X, k_Y) = k \times (u/f_o, v/f_o)$ , where k is the wavenumber and  $k_X$  or  $k_Y \equiv k_{\parallel}$ , the in-plane momentum. The field distribution in this plane is relayed to the entrance plane of the spectrometer using a pair of lenses L250 (f = 250 mm) and L200 (f = 200 mm). In the conjugate real-space imaging plane (r-space), we place a 600- $\mu$ m diameter circular aperture to spatially isolate luminescence and a single transverse mode within a circular  $\approx 10$ - $\mu$ m diameter area on the sample. The image at the entrance plane can be directed to the LN-CCD for time-integrated imaging/spectroscopy or to the streak camera system for time-resolved measurements. In this configuration, we measure the angular distribution of luminescence as k-space images (k-images) or spectra (E vs.  $k_{\parallel}$  dispersions) using respectively the 0-order or 1st-order diffracted light from the grating. By inserting a removable 200 mm focal-length lens (L200), we project the r-space luminescence to the entrance plane of the spectrometer. Notice that a miniature mirror is positioned to direct the pump beam at an incident angle  $\approx 20^{\circ}$  in front of the objective. This mirror partially blocks the reflected luminescence near a corner shown nearby the spectrometer.

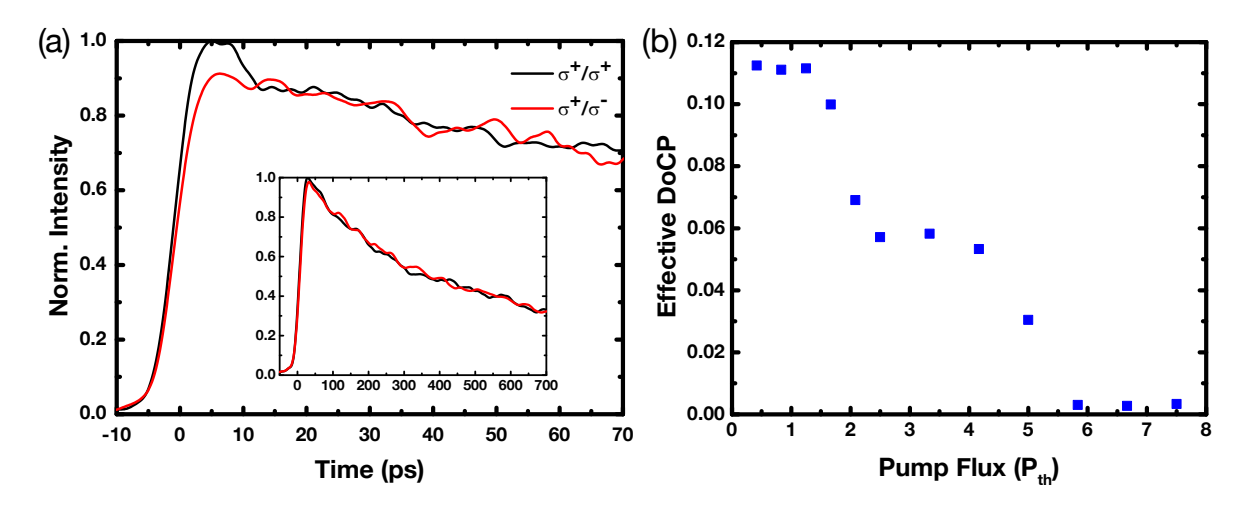


Fig. S4. Time-dependent polarized PL in InGaAs/GaAs MQWs. To investigate the photoluminescence (PL) and spin dynamics in InGaAs/GaAs MQWs in the absence of a cavity, we measure time-dependent polarized PL in a sample with all top DBR layers removed by selective wet etching. (a) Time-resolved polarized PL  $I^{\pm}(t)$  (black lines:  $I^{+}(t)$ , co-circular  $\sigma^{+}/\sigma^{+}$ component; red lines:  $I^-(t)$ , cross-circular  $\sigma^+/\sigma^-$ ). Time-dependent  $DoCP \rho_c(t)$  has a finite value of 0.12 when PL intensity increases to its maximum in about 10 ps, and then decays rapidly with a spin relaxation time  $\tau_s < 10$  ps. On the other hand, the carrier decay time is much larger,  $\tau_n \sim 1$  ns, as deduced from the overall decay of time-dependent PL intensity I(t) (inset). (b) Effective initial stationary DoCP,  $\bar{\rho}_c^* = \int_{t=0}^{t=10 \text{ ps}} \frac{I^+(t) - I^-(t)}{I^+(t) + I^-(t)} dt$ , as a function of pump flux. We determine  $\bar{\rho}_c^*$  to be always less than 0.1 in InGaAs MQWs with similar photoexcited e-h carrier densities. The instantaneous carrier density excited in the InGaAs MQWs after pulse excitation is proportional to P. We thus scale P in units of  $P_{th}$ , which is the threshold pump flux in an as-grown microcavity sample with top DBR layers. The photoexcited density at  $P_{th}$  is  $\sim 2-3\times 10^{12}$  cm<sup>-2</sup> per quantum well per pulse. The diminishing  $\bar{\rho}_c^*$  with increasing pump flux above 2  $P_{th}$  suggests that the spin relaxation time  $\tau_s$ decreases further as compared to carrier lifetime  $\tau_n$  at high photoexcited densities, owing to increasingly dominant spin-flipping carrier-carrier scatterings. We emphasize that  $\tau_s$  is less than 10 ps at the threshold photoexcited density and decrease even further at higher densities. The spin relaxation dynamics measured in InGaAs MQWs with and without the top DBR layers below the threshold photoexcited density are consistent, confirming that the spin relaxation in MQWs is not affected by the presence of cavity below threshold.

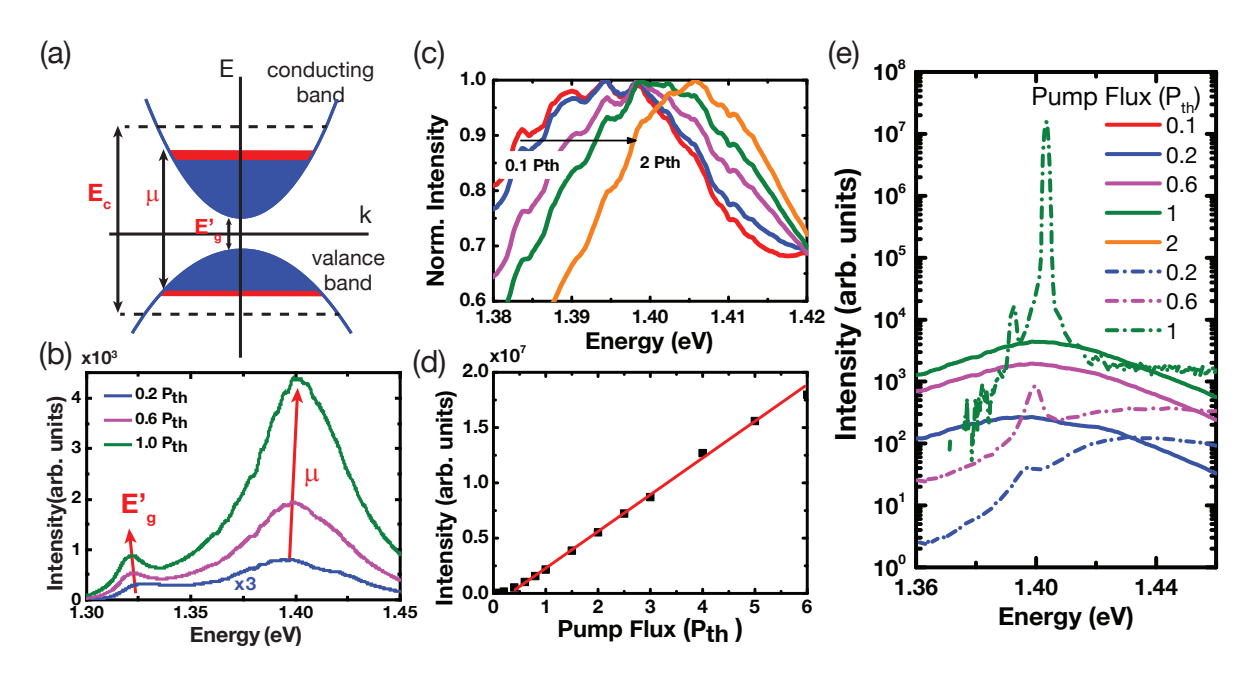


Fig. S5. Density-dependent PL in InGaAs/GaAs MQWs. To determine the density-dependent spectral characteristics of PL in InGaAs/GaAs MQWs, we measure time-integrated PL in the sample with top DBR mirror layers removed (same as Fig. S4). (a) Schematic of simplified energy bands in InGaAs/GaAs MQWs. Phase-space filling of electrons and holes (blue painting area) advances the chemical potential  $(\mu)$  towards the cavity resonance  $E_c$ . A fraction of e-h pairs near Fermi-edge (red area) can couple effectively to the cavity light field. The QW-bandgap  $(E'_g)$  corresponds to the ground state, 1e-1hh (electron to heavy-hole) transition.  $E'_q$  can decrease with increasing photoexcited density (band gap renormalization). (b) PL spectra at P = 0.2 (blue), 0.6 (magenta) and 1  $P_{th}$  (green). Here, PL is attributed to spontaneous radiative recombination of photoexcited carriers in InGaAs/GaAs MQWs. The dual PL spectral peaks are attributed to the ground and first excited state in MQWs, respectively.  $E'_g$  is associated with the ground state, while  $\mu$  can be deduced from PL from the excited state. With increasing density,  $E'_g$  redshifts slightly owing to band gap renormalization, while  $\mu$  blueshifts considerably owing to phase space filling (Pauli blocking).  $\mu$  reaches approximately 80 meV above  $E'_g$  at such a high photoexcited density ( $\gtrsim 10^{12}$  cm<sup>-2</sup> per QW). (c) Normalized PL spectra near 1.40 eV, displaying a significant spectral blueshift of 15-20 meV with increasing photoexcited density (0.1 to 2  $P_{th}$ ). (d) The spectrally integrated PL emission flux  $I_{PL}$ . In the absence of the top DBR mirror layers, no lasing is expected and  $I_{PL}$  increases linearly with pump flux for  $P \approx 0.2 P_{th}$  up to 6  $P_{th}$ . (e) Comparisons of selected PL spectra with (dashed lines) and without (solid line) the top DBR mirror layers. In the as-grown microcavity sample, below the threshold density, PL is dominated by spectrally broad background emissions centering at 1.44 eV is from GaAs spacer layers when radiative recombination of carriers InGaAs MQWs is suppressed. Above threshold, emissions near the cavity resonance increase dramatically by 3-4 orders of magnitude as compared to that in the absence of the top DBR mirror. The quantum efficiency of radiative recombination is enhanced, owing to stimulation of correlated e-h pairs emerging from the coupling to the cavity light field.

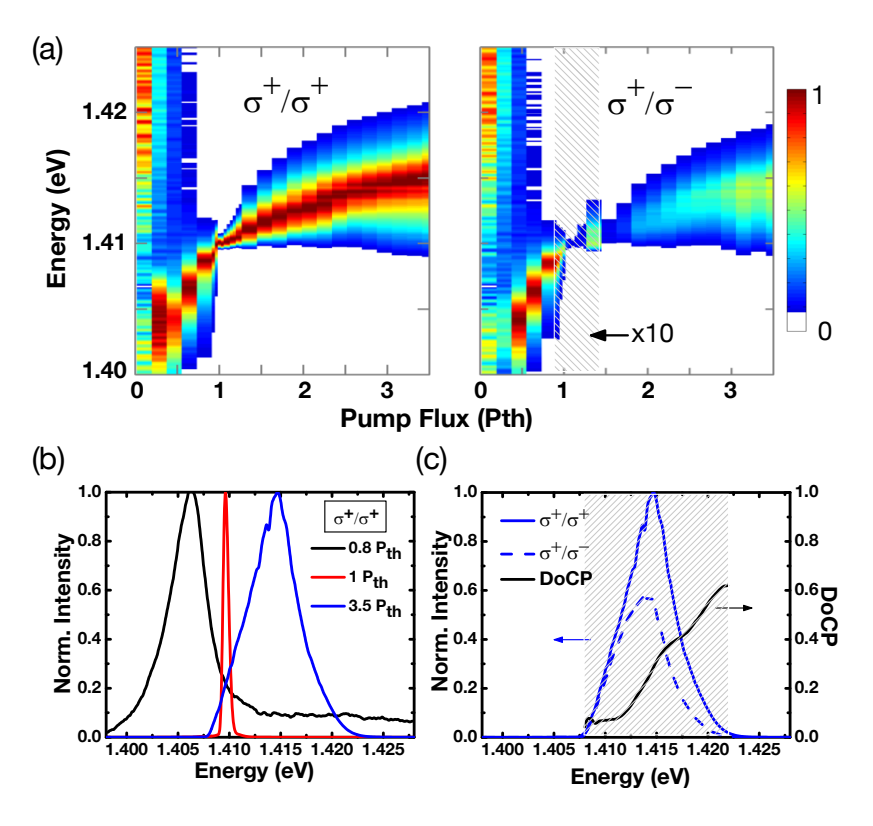


Fig. S6. Time-integrated polarized spectra. (a) Two-dimensional (2D) false-color images of microcavity luminescence/lasing spectra vs. pump flux for co-circular ( $\sigma^+/\sigma^+$ , left panel) and cross-circular ( $\sigma^+/\sigma^-$ , right panel) components. Spectra are normalized with respect to the co-circular component  $(\sigma^+/\sigma^+)$  for each pump flux. Note that the intensities of  $\sigma^+/\sigma^-$  spectra for 0.8  $P_{th} < P < 1.3$   $P_{th}$  (shaded area) are scaled up by a factor of 10. Far below threshold  $(P \ll 0.2 P_{th})$ , we see only spectrally broad luminescence ( $\Delta E > 30 \text{ meV}$ ,  $\bar{E} \sim 1.425 \text{ eV}$ ) from the GaAs spacer layers. Slightly below threshold  $(0.2 - 0.5 P_{th} < P < P_{th})$ , luminescence from the radiative recombination of carriers in InGaAs MQWs becomes visible at ~1.405 eV and gradually dominates over that from GaAs layers. Such luminescence comes from the resonant modes built from the e-h near Fermi-edge coupling to cavity resonance  $E_c$  as  $\mu \to E_c$  with increasing photoexcited carriers in MQWs. In particular, a parabolic E vs.  $k_{\parallel}$  dispersive curve consisting of spectrally narrower peaks ( $\Delta E < 5$  meV) appears, which similar to E-k dispersion can see the non-lasing spectrum in Fig. 1 (b)  $(\sigma^+/\sigma^- \text{ component})$  in paper. Slightly above lasing threshold  $(P_{th} < P < 1.5 P_{th})$ , spectrally narrow radiation emerges ( $\Delta E \approx 0.3 - 1.0 \text{ meV}$ ) with high DoCP. Far above threshold  $(1.5 P_{th} < P)$ , luminescence exhibits spectral broadening with linewidth more than 2 meV, energy blueshift up to 5 meV and decreasing average DoCP with increasing pump flux. (b) Selected co-circular time-integrated polarized spectra for P=0.8(black), 1.0 (red) and 3.3 (blue)  $P_{th}$ . Spectral blueshifts and linewidth broadening with increasing pump flux can be readily identified in these selected spectra. (c) Polarized time-integrated spectra (blue solid line: co-circular; blue dashed line: crosscircular) and spectral DoCP [ $\bar{\rho}(E)$ , black line] for  $P=3.5~P_{th}$ . The spectral broadening observed such time-integrated spectra is partly due to the temporal evolution of emission peaks towards  $E'_q$  (Fig. 4c and Fig. S7). The diminishing  $\bar{\rho}(E)$  with decreasing energy corroborates the temporally descending  $\mu$  and diminishing spin-imbalance of correlated e-h pairs near the Fermi edge. Spin-dependent stimulation leads to buildup of a spin-polarized coherence state and consequent polarized laser radiation. The buildup time of such a coherent state is inversely proportional to the initial occupation of spin-polarized correlated e-hpairs. Consequently, inceptive laser radiation appears at higher energy and is circularly polarized. With increasing time delay after pulse excitation, spin-imbalance diminishes due to the continuing spin-flipping, while  $\mu$  ascends due to the rapid depletion of reservoir e-h carriers. Therefore, the laser radiation appears at descending energy with diminishing circular polarization with time. The time-integrated spectra would then display an apparent spin-dependent energy splitting of 1-2 meV.

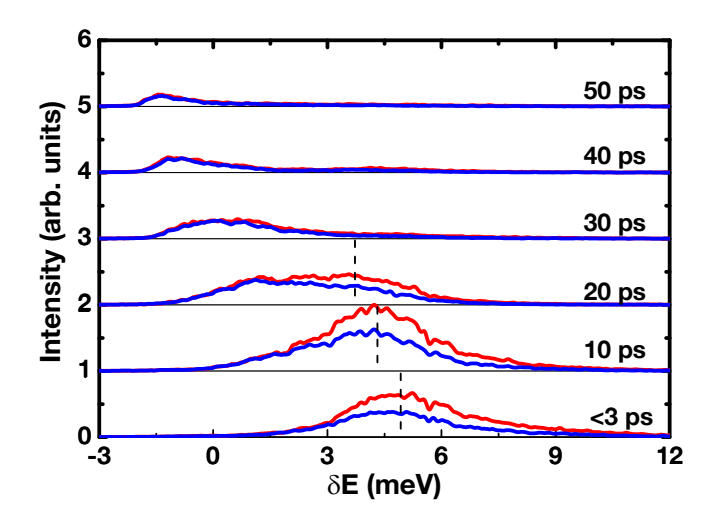


Fig. S7. Transient lasing spectra at  $P=4\,P_{th}$ . Cross-sectional transient spectra at specified time delays extracted from the temporally and spectrally-resolved streak images of a sample. Transient spectra are averaged over 5 ps and normalized to the maximal peak intensity of the co-circular component. The spectra are equally scaled but offset vertically by 1. Red lines represent the co-circular  $(\sigma^+/\sigma^+)$  component, while blue lines represent the cross-circular  $(\sigma^+/\sigma^-)$  one. The energy scale is measured with respect to 1.408 eV, which is the peak lasing energy at the threshold  $P_{th}$ . In initial time delay of few ps after pulse excitation, the emission is spectrally broad and blueshifts by about 5 meV. For delays less than 20 ps, the co- and cross-circular components have the same spectral peak energy (vertical dashed lines), suggesting carriers interactions with same spins and opposite spins are in comparable magnitude. The spectral peak energy is determined by the total carrier density instead of individual spin-up or spin-down population. On the other hand, the intensity of the co-circular component is higher than the cross-circular component within 20 ps after pulse excitation because the ineffective spin-flipping in reservoir results in imbalance spin-population. The emission spectrum reaches a maximum at about 10 ps, and then gradually decreases in overall magnitude and redshifts with time. The temporal energy redshift in spectra is attributed to a descending chemical potential  $\mu$  with a decreasing carrier density.

### THEORETICAL MODEL: SPIN-DEPENDENT STIMULATION

To model the spin-controlled lasing processes, we adapt a set of rate equations with spin-dependent stimulated processes. We consider two states populated with spin-polarized electron-hole (e-h) pairs: non-radiative e-h plasma reservoir  $(M_{eh}^{\pm})$ , and radiative correlated e-h pairs at  $k_{\parallel}\approx 0$   $(n_{0}^{\pm})$ . The e-h pairs photoexcited by a 2-ps pulsed pump laser non-resonantly at 1.58 eV relax rapidly (<5 ps) to the reservoir via, for example, spin-preserved scattering process with LO optical phonons. Therefore, we assume that spin-polarized e-h pairs are optically injected into the reservoir at a generation rate of  $G_pP^{\pm}$ , where  $P^{\pm}$  is the pump laser flux of helicity  $\pm$ . The spin flipping time of e-h pairs,  $1/W_{sf}$ , is less than 10 ps, as demonstrated by the polarized time-dependent PL below threshold (Fig. 4) as well as in a sample without the top DBR mirror layers (Fig. S5). The e-h carriers in the reservoir can also dissipate through reabsorption and non-radiative recombination ( $\Gamma_{loss}$ ). We further assume that a fraction of e-h pairs near the Fermi-edge couple effectively to the cavity light field, forming correlated e-h pairs  $(N_{eh}^{\pm}=\beta M_{eh}^{\pm})$ . The conversion of carriers from  $N_{eh}$  to the radiative  $n_0$  state is enabled by the following processes: (a)  $W_k$ , a spontaneous conversion from  $N_{eh}$ , and (b)  $W_{ss}$ , spin-dependent stimulated scattering from  $N_{eh}$ . The  $n_0$  state contributes to the leakage photons measured experimentally at a rate associated with the cavity photon decay rate  $\Gamma_c$ . The lasing dynamics can then be described by the following set of coupled rate equations:

$$\frac{d M_{eh}^{\pm}(t)}{dt} = G_p(t) P^{\pm} \mp W_{sf} \left[ M_{eh}^{+}(t) - M_{eh}^{-}(t) \right] - \Gamma_{loss} M_{eh}^{\pm}(t) - W_{ss}(n_0^{\pm}) N_{eh}^{\pm}(t) n_0^{\pm}(t) - W_k N_{eh}^{\pm}(t) , \qquad (1)$$

$$\frac{d n_0^{\pm}(t)}{dt} = W_{ss}(n_0^{\pm}) N_{eh}^{\pm}(t) n_0^{\pm}(t) + W_k N_{eh}^{\pm}(t) - \Gamma_c n_0^{\pm}(t).$$

The generation rate of carriers,  $G_p(t)$ , from a 2-ps pulsed laser pump is represented by a Gaussian distribution with a standard deviation  $\sigma = 2$  ps. The spin-dependent stimulation rate  $W_{ss}$  is phenomenologically set to decrease above a saturation density,  $n_{sat}$ , which is obtained by fitting the pump-flux dependent stationary DoCP ( $\bar{\rho_c}$ ):

$$W_{ss} = \begin{cases} W_0 &, \text{ when } n_0^{\pm} < n_{sat} \\ W_0 \times [1 - \lambda(n_0^{\pm} - n_{sat})] &, \text{ when } n_0^{\pm} \ge n_{sat}. \end{cases}$$
 (2)

The fittings parameters are as follows:  $W_0 = 1/10 \text{ [ps}^{-1]}$ ,  $W_{sf} = 1/10 \text{ [ps}^{-1]}$ ,  $W_k = 10^{-4} \text{ [ps}^{-1]}$ ,  $\Gamma_{loss} = 1/1000 \text{ [ps}^{-1]}$ ,  $\Gamma_c = 1 \text{ [ps}^{-1]}$ ,  $\beta = 0.015$ ,  $\lambda = 0.007$ , and  $n_{sat} = 20$  (corresponding to the occupation number of state  $n_0$  at  $P = 1.5 P_{th}$ ). Given a spatial mode area of 10-20  $\mu\text{m}^2$  for the  $n_0$  state, the calculated threshold density is about  $5 - 10 \times 10^5 \ \mu\text{m}^{-2}$ , consistent with experimentally measured carrier density per quantum well at threshold. This model reproduces the polarized laser output fluxes  $(I^{\pm})$  and DoCP ( $\bar{\rho}_c$ ) as a function of pump flux P (Fig. 2) and as a function of pump polarization  $\rho_c^p$  (Fig. 3 and Fig. S8a). The polarized time-dependent PL is also reproduced qualitatively [Fig. S8(b-c)].

We note a few shortcomings of this simplified model: (1) It does not consider energy relaxation and spatial carrier diffusion properly. As a result, the spectral dependent stationary  $\bar{\rho}_c(E)$  and time-resolved  $\rho_c(E,t)$  cannot be reproduced. (2) The model does not consider optical selection rules under a non-resonant optical pumping and neglects the fact that hole spin relaxation time is sub-ps. In InGaAs/GaAs quantum wells, the initial  $\rho_c$  of the band-edge PL is limited to 0.25 due to sub-ps hole spin relaxation for a non-resonant optical excitation with more than 150 meV excess energy in our experiments, whereas the model gives a  $\rho_c(t=0)=1$ . Therefore, the model produces a stationary  $\bar{\rho}_c$  higher than experimental values below threshold. Moreover, the calculated  $\bar{\rho}_c$  across the threshold is smooth, in contrast to the "step-like" increase with increasing pump flux in the experiments. (3) We model the saturation effect by a weak linear decrease of stimulated scattering rate  $W_{ss}$  when the density  $n_0$  is increased above a saturation density  $(n_{sat})$ . The  $W_{ss}(n_0)$  can exhibit a more complex density dependence when energy relaxation and spectral broadening of the lasing mode are considered. Although the model exists shortcomings aforementioned, this simplified one could qualitatively simulate main experimental results including polarization amplification under elliptically polarized pumping and spin-polarized pulsed lasing dynamics.

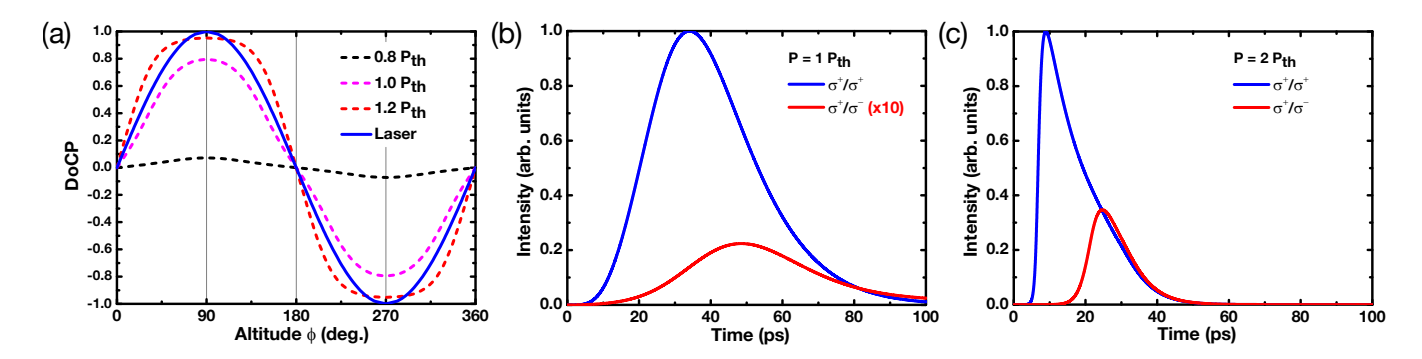


Fig. S8. **Spin-dependent Stimulation.** (a) Calculated stationary  $DoCP(\bar{\rho_c})$  with varying pump polarization  $\rho_c^p$  (represented by the altitude) for P=0.8, 1.0 and 1.2  $P_{th}$ . (b-c) Calculated polarized time-dependent radiation intensity for co-circular  $\sigma^+/\sigma^+$   $[I^+(t)]$  and cross-circular  $\sigma^+/\sigma^+$   $[I^-(t)]$  components under a  $\sigma^+$  pump for P=1.0 and 2.0  $P_{th}$ . The theoretical  $P_{th}$  is set to when the stationary  $\bar{\rho_c}=0.5$  under a fully circularly polarized pump  $(\rho_c^p=1)$ .